Supporting Information

Rational design of carbon nanocomposites with the hierarchical porosity: a strategy to improve capacitive energy storage performance

Agnieszka Hryniewicka[1], Joanna Breczko[1,2], Gabriela Siemiaszko[1], Krzysztof Brzezinski[3], Anna Ilnicka[4], Artur P. Terzyk[4], and Marta E. Plonska-Brzezinska[1*]*

[1] Department of Organic Chemistry, Faculty of Pharmacy with the Division of Laboratory Medicine, Medical University of Bialystok, Mickiewicza 2A, 15-222 Bialystok, Poland

[2] Faculty of Chemistry, University of Bialystok, Ciolkowskiego 1K, 15-245 Bialystok, Poland

[3] Department of Structural Biology of Prokaryotic Organisms, Institute of Bioorganic Chemistry, Polish Academy of Sciences, Noskowskiego 12/14, 61-074 Poznan, Poland

[4] Faculty of Chemistry, Nicolaus Copernicus University in Torun, Gagarin Street 7, 87-100 Torun, Poland

Table of contents

METHODS..... 3

Figure S1. ^{1}H NMR spectrum of 1,4-bis(6-methylbenzo[d]thiazole-2-yl)-2,5-bis(4-cyanophenyl)-1,4-dihydropyrrolo[3,2-b]pyrrole (**2CN-2**)..... 7

Figure S2. ^{13}C NMR spectrum of 1,4-bis(6-methylbenzo[d]thiazole-2-yl)-2,5-bis(4-cyanophenyl)-1,4-dihydropyrrolo[3,2-b]pyrrole (**2CN-2**)..... 7

Figure S3. High-resolution mass spectrum of spectrum of 1,4-bis(6-methylbenzo[d]thiazole-2-yl)-2,5-bis(4-cyanophenyl)-1,4-dihydropyrrolo[3,2-b]pyrrole (**2CN-2**)..... 8

Figure S4. High-resolution mass spectrum of 1,2,4,5-tetrakis(4-cyanophenyl)-1,4-dihydropyrrolo[3,2-b]pyrrole (**4CN-2**). 8

Table S1. Surface elemental composition of carbon samples determined by XPS and elemental analysis results..... 9

Figure S5. XPS spectra of the C 1s spectral region of the CTF and CTF-CNO materials. 10

Figure S6. ^{13}C CP-MAS NMR spectra of the CTF and CTF-CNO materials. 11

Table S2. Chemical state, positions, FWHM, and relative area percentages of the deconvoluted C 1s peaks from the XPS analyses of CTF materials. 12

Table S3. Chemical state, positions, FWHM, and relative % area of the deconvoluted C 1s peaks from the XPS analyses of CTF-CNO materials. 12

Table S4. Chemical state, positions, FWHM, and relative area percentages of the deconvoluted N 1s peaks from XPS analyses of CTF materials. 13

Table S5. Chemical state, positions, FWHM, and relative % area of the deconvoluted N 1s peaks from XPS analyses of CTF-CNO materials. 13

Figure S7. The differential pore size distribution of CTF and CTF-CNO materials..... 14

Figure S8. The cumulative pore volume of CTF and CTF-CNO materials…….14

Figure S9. Nyquist plots obtained for GCE electrodes covered with (a) CTF and (b) CTF-CNO materials at 0.4 V. (c) EIS spectra recorded for GCE modified with CTF-4CNO-1-CNO at different potentials and electrical equivalent circuit (inset)…….15

Figure S10. TGA/DSC analysis of the selected pristine CTF and CTF-CNO materials. Analysis was performed in an air atmosphere…….16

Table S6. Electrochemical properties of porous carbon materials containing triazines and carbon nanostructures. ……..17

References 21

METHODS

High-resolution transmission electron microscopy (HRTEM) was performed using a Titan G2 HRTEM microscope that was operated at 300 kV (FEI company) equipped with a field emission (FEG) gun. HRTEM imaging of the sample microstructure was performed in bright field mode using a CCD camera as a detector.

^{1}H and ^{13}C NMR spectra were recorded on an Agilent VNMRS system that was operated at 500 MHz for ^{1}H NMR and 126 MHz for ^{13}C NMR. The chemical shifts δ are given in ppm, are in reference to the solvent peak of $CDCl_3$, and are defined at δ 7.26 (^{1}H NMR) or δ 77.16 (^{13}C NMR). The following abbreviations were used for multiplicities: s (singlet), d (doublet), m (multiplet). ^{13}C CP-MAS NMR spectra were performed using Bruker Avance III 400 Wide Bore (9,4 T). The elemental analysis was performed using the Elementar Unicube CHNS analyzer.

High-resolution mass spectra were acquired using a MALDISynapt G2-S HDMS (Waters Corporation, Milford, MA, USA) coupled to a Waters TQD mass spectrometer (electrospray ionization mode ESI-tandem quadrupole).

Fourier transform infrared (FTIR) spectroscopy was performed using a Thermo Scientific Nicolet IN10 MX microscope (USA). The spectra were recorded with a KBr pellet using a microscope in transmission mode. The spectra were collected at a resolution of 4 cm^{-1}, and 64 scans were averaged to obtain a single spectrum.

For X-ray powder diffraction (XRD), the samples were loaded into glass capillaries (Hampton Research, Glass Number 50) with a diameter of 0.5 mm. The XRD data were measured using CuKα radiation at 25 °C on an XtalLAB Synergy diffractometer (Rigaku) equipped with the Hybrid Pixel 2-dimensional detector HyPix-6000HE. For all experiments, the sample-to-detector distance was set to 148 mm, and the data were recorded over a 2θ

angle range from 10° to 100° using the standard phi scan procedure. In all experiments, the exposure time was 60 seconds.

X-ray photoelectron spectroscopy (XPS) was performed using an ultrahigh-vacuum (UHV) chamber (PREVAC) (base pressure below 10-8 mbar) with a nonmonochromatic AlKα (1486.7 eV; 12 kV; 30 mA) radiation source (VG Scienta SAX 100) and monochromator (VG Scienta XM 780). The emitted photoelectrons were detected using a Scienta R4000 hemispherical analyzer. For all samples, a low-resolution survey run (0–1350 eV) at a pass energy of 200 eV was performed. The C 1s and N 1s high-resolution spectra were recorded at a pass energy of 20 eV at room temperature. The C 1s and N 1s spectra were fitted by Gaussian–Lorentzian functions after Shirley background subtraction was performed. The peaks were fitted using CasaXPS software (Casa Software Ltd.). The C KLL spectra (XAES) were obtained by XPS. The first-derivative XAES spectra were obtained using a 25-point Savitzky–Golay quadratic polynomial differentiation method.

Nitrogen adsorption-desorption isotherms (-196 °C) were measured using an ASAP 2020 Plus 2.00A (Micromeritics, USA) adsorption apparatus. Before the adsorption-desorption measurements were performed, all the samples were subjected to vacuum evacuation at 200 °C for at least 24 h.

A PGSTAT 302N potentiostat (Autolab B.V., Metrohm, Utrecht, the Netherlands) connected to a three-electrode system (working glassy carbon electrode (GCE, 10 x 2 mm), a silver/silver chloride reference electrode and an auxiliary platinum mesh electrode) or to a two-electrode system (two identical glassy carbon electrodes (GCE, 10 x 2 mm)) was used in voltammetric (CV) and galvanostatic (GCD) measurements, respectively. Electrochemical impedance spectroscopy (EIS) measurements were also performed in three-electrode configuration. EIS spectra were recorded using a 5 mV amplitude. All EIS spectra were recorded over the frequency range of 0.1 Hz to 10 kHz at open circuit potential (OCP). Before the measurements, the surface of the GCE electrode was polished by alumina (0.3 mm) and

diamond (0.25 mm) paste and modified by deposition of 15 μL of a solution containing CTF or CTF-CNO material dispersed in ethanol (3 mg mL^{-1}) with the addition of 1 mg of conductive carbon paint (CP, SPI Supplies, USA) as a binder. The modification was complete when the solvent was evaporated at RT. The measurements were performed at the room temperature. The calculated electrode mass loading was about 0.86 mg/cm^2. We performed at least 10 replicates for each electrochemical measurement. The CV, GCD, and EIS studies show representative curves for each group of measurements. Where calculated values for these methods are given, they are averaged, and the standard deviation is given for CVs: 10 measurements; GCD and EIS: 5 measurements. All electrochemical analyses were performed in a 1 M H_2SO_4 solution.

In order to calculate specific capacitance, specific energy and specific power values the appropriate formulas were used.

For CV calculations:

$$C_s = \frac{\int_{V_1}^{V_2} i(V)dV}{2vm(V_2 - V_1)}$$

where: $\boldsymbol{C_s}$ - specific capacitance, $\boldsymbol{i}$ - current, $\boldsymbol{v}$ – scan rate, $\boldsymbol{m}$ - mass of material, $\boldsymbol{V}$ - potential

For GCD calculations:

$$C_s = \frac{it_d}{m\Delta V}$$

$$\boldsymbol{E_S} = \frac{\boldsymbol{C_s} \cdot (\Delta \boldsymbol{V})^2}{\boldsymbol{2 \cdot 3.6}}$$

$$\boldsymbol{P_S} = \frac{\boldsymbol{3600 \cdot E_S}}{\boldsymbol{t_d}}$$

where: $\boldsymbol{C_s}$ - specific capacitance, $\boldsymbol{i}$ - current, $\boldsymbol{t_d}$ - time of discharge, $\boldsymbol{m}$ - mass of material, $\Delta \boldsymbol{V}$ -potential difference, $\boldsymbol{E_S}$ – specific energy, $\boldsymbol{P_S}$ – specific power.

E_S and P_S were calculated were calculated from the mean values of the GCD measurements given in Table 2.

^{1}H NMR and ^{13}C NMR SPECTROSCOPY

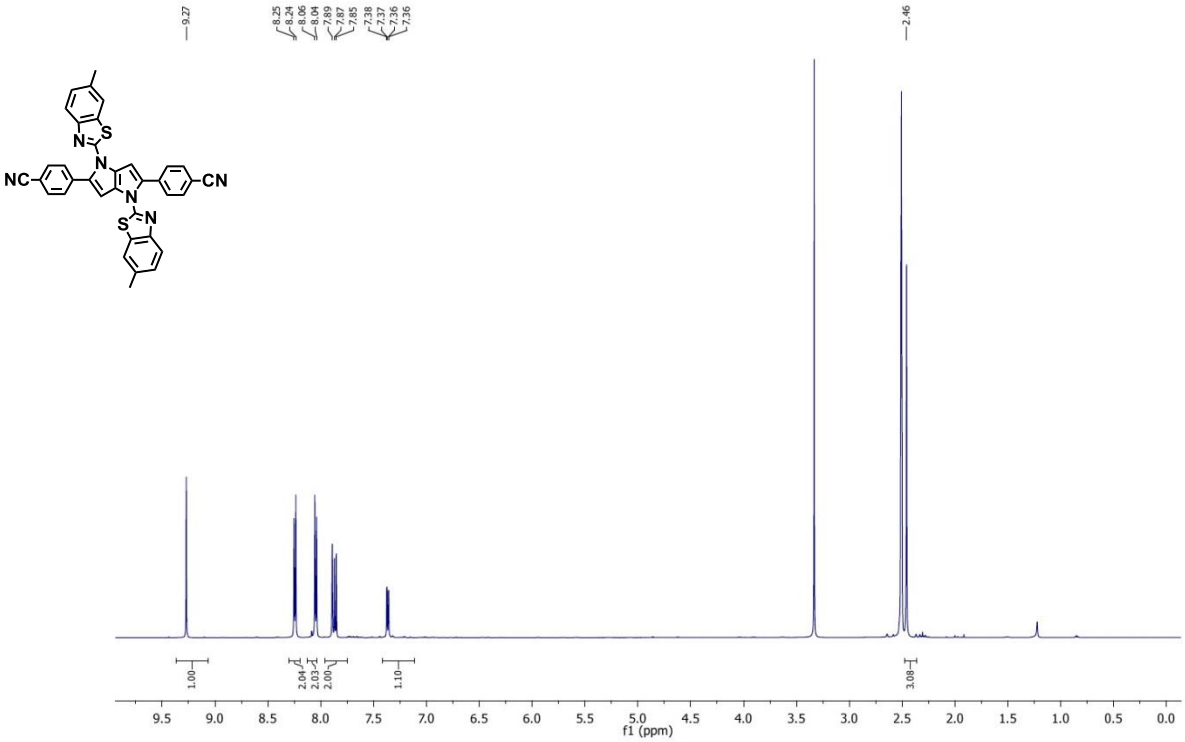

Figure S1. ^{1}H NMR spectrum of 1,4-bis(6-methylbenzo[d]thiazole-2-yl)-2,5-bis(4-cyanophenyl)-1,4-dihydropyrrolo[3,2-b]pyrrole (2CN-2).

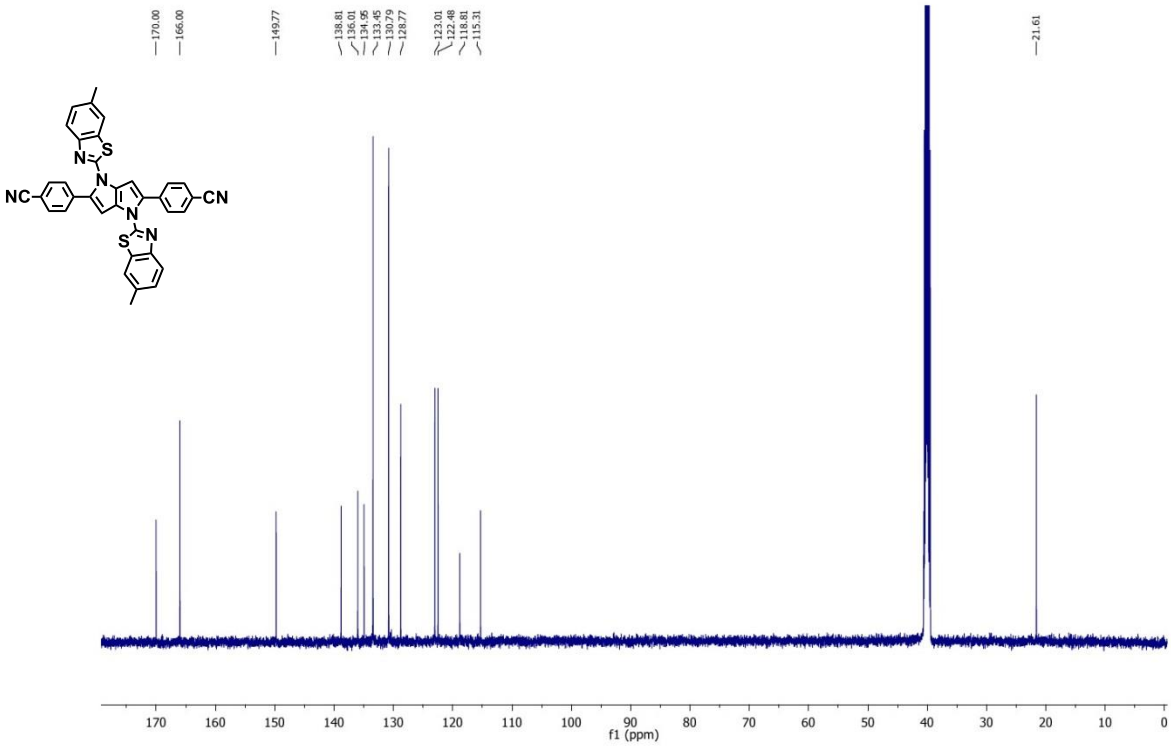

Figure S2. ^{13}C NMR spectrum of 1,4-bis(6-methylbenzo[d]thiazole-2-yl)-2,5-bis(4-cyanophenyl)-1,4-dihydropyrrolo[3,2-b]pyrrole (2CN-2).

MASS SPECTROMETRY

Single Mass Analysis
Tolerance = 3.0 mDa / DBE: min = -1.5, max = 300.0
Element prediction: Off
Number of isotope peaks used for i-FIT = 3
Monoisotopic Mass, Even Electron Ions
50 formula(e) evaluated with 1 results within limits (up to 50 closest results for each mass)
Elements Used:
C: 0-300 H: 0-300 N: 0-6 S: 2-2

Mass	Calc. Mass	mDa	PPM	DBE	Formula	i-FIT	i-FIT Norm	Fit Conf %	C	H	N	S
603.1434	603.1426	0.8	1.3	28.5	C36 H23 N6 S2	65.3	n/a	n/a	36	23	6	2

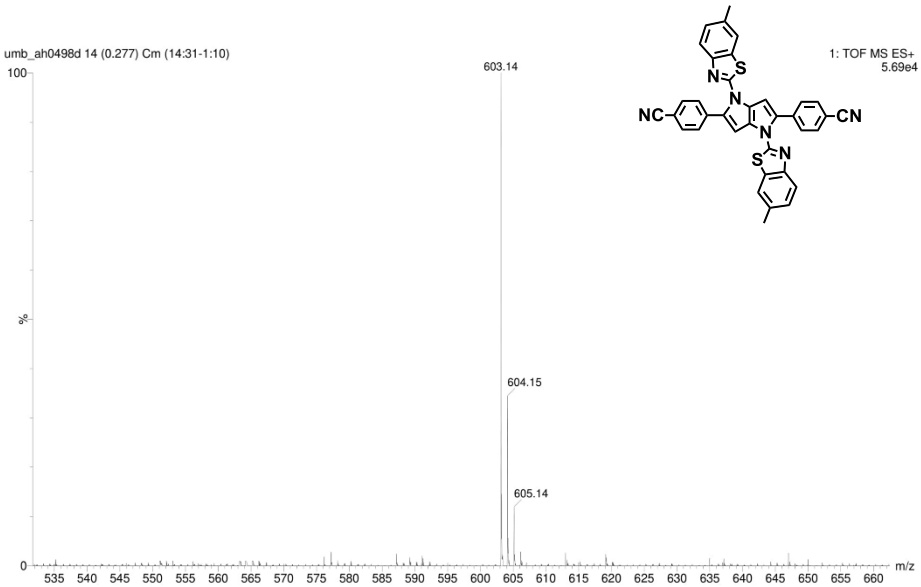

Figure S3. High-resolution mass spectrum of spectrum of 1,4-bis(6-methylbenzo[d]thiazole-2-yl)-2,5-bis(4-cyanophenyl)-1,4-dihydropyrrolo[3,2-b]pyrrole (2CN-2).

Single Mass Analysis
Tolerance = 3.0 mDa / DBE: min = -1.5, max = 500.0
Element prediction: Off
Number of isotope peaks used for i-FIT = 3
Monoisotopic Mass, Odd and Even Electron Ions
46 formula(e) evaluated with 1 results within limits (all results (up to 1000) for each mass)
Elements Used:
C: 0-100 H: 0-100 N: 0-6

Mass	Calc. Mass	mDa	PPM	DBE	Formula	i-FIT	i-FIT Norm	Fit Conf %	C	H	N
510.1596	510.1593	0.3	0.6	29.0	C34 H18 N6	362.2	n/a	n/a	34	18	6

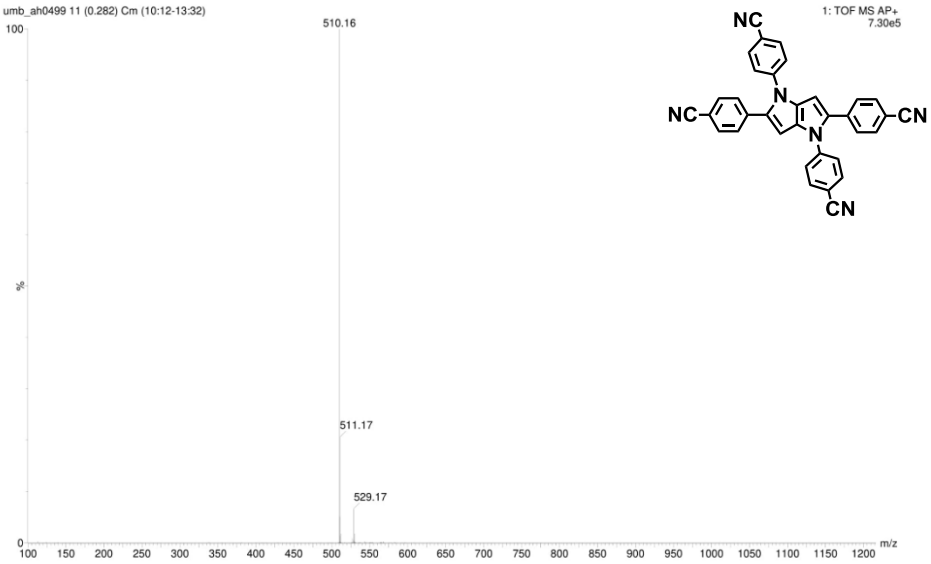

Figure S4. High-resolution mass spectrum of 1,2,4,5-tetrakis(4-cyanophenyl)-1,4-dihydropyrrolo[3,2-b]pyrrole (4CN-2).

X-RAY PHOTOELECTRON SPECTROSCOPY and ELEMENTAL ANALYSIS

Table S1. Surface elemental composition of carbon samples determined by XPS and elemental analysis results.

Sample	XPS analysis			Elemental analysis			
	Elements (%)			Elements (%)			
	C	N	other	C	H	N	S
CTF-2CN-1	86.5	6.6	6.8	64.63	1.50	6.98	-
CTF-2CN-1-CNO	85.3	8.1	6.6	65.16	2.17	9.38	-
CTF-2CN-2	81.6	5.4	13	55.56	1.11	5.28	9.23
CTF-2CN-2-CNO	90.9	4.8	4.2	66.89	1.25	5.49	11.36
CTF-4CN-1	86.5	7.5	6	67.28	1.70	7.56	-
CTF-4CN-1-CNO	84.1	9.5	6.4	65.33	2.26	9.76	-
CTF-4CN-2	85.7	6.5	7.7	71.38	1.36	7.53	-
CTF-4CN-2-CNO	89.9	4.3	5.7	73.34	1.76	6.25	-

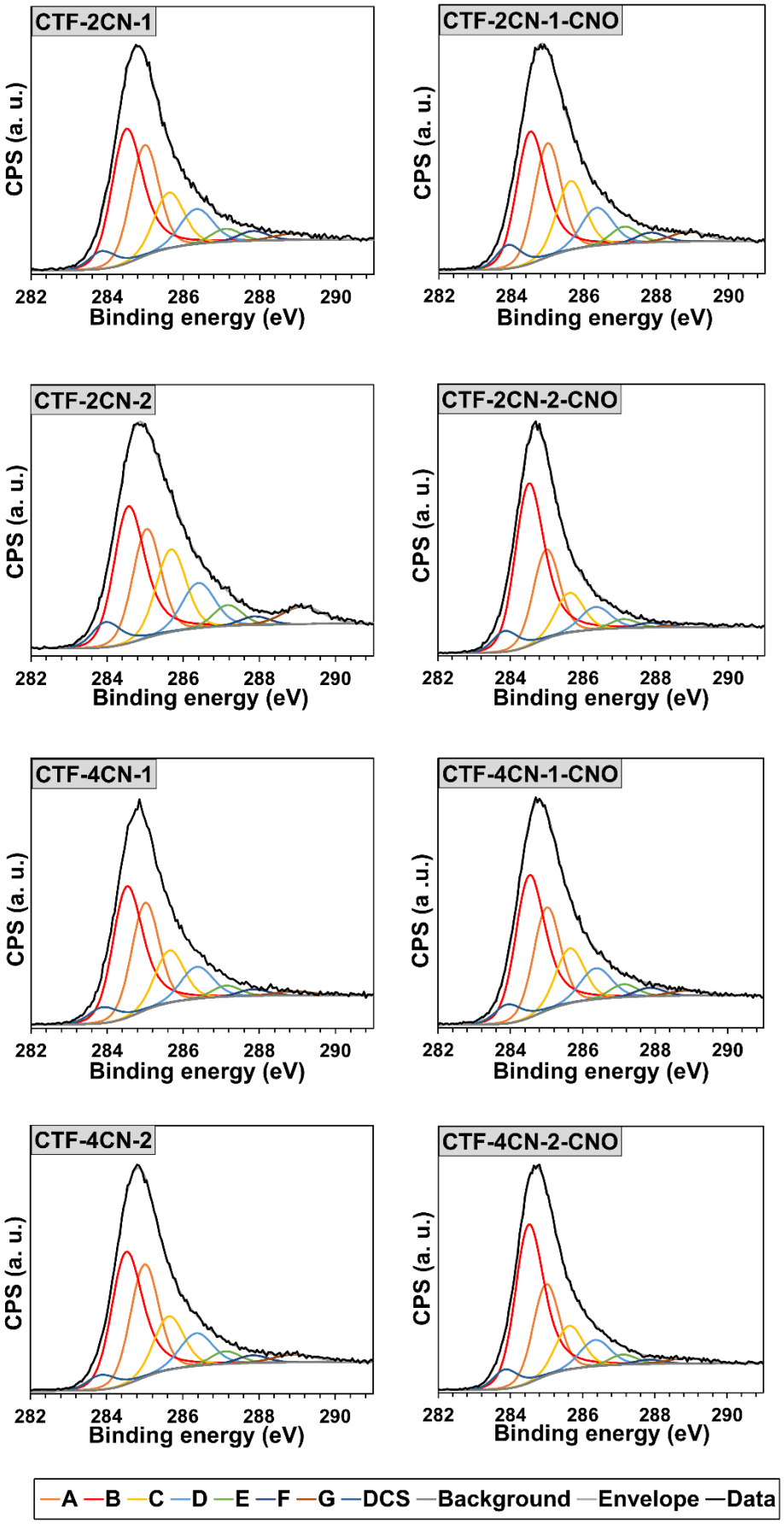

Figure S5. XPS spectra of the C 1s spectral region of the CTF and CTF-CNO materials.

CP-MAS ^{13}C NMR SPECTROSCOPY

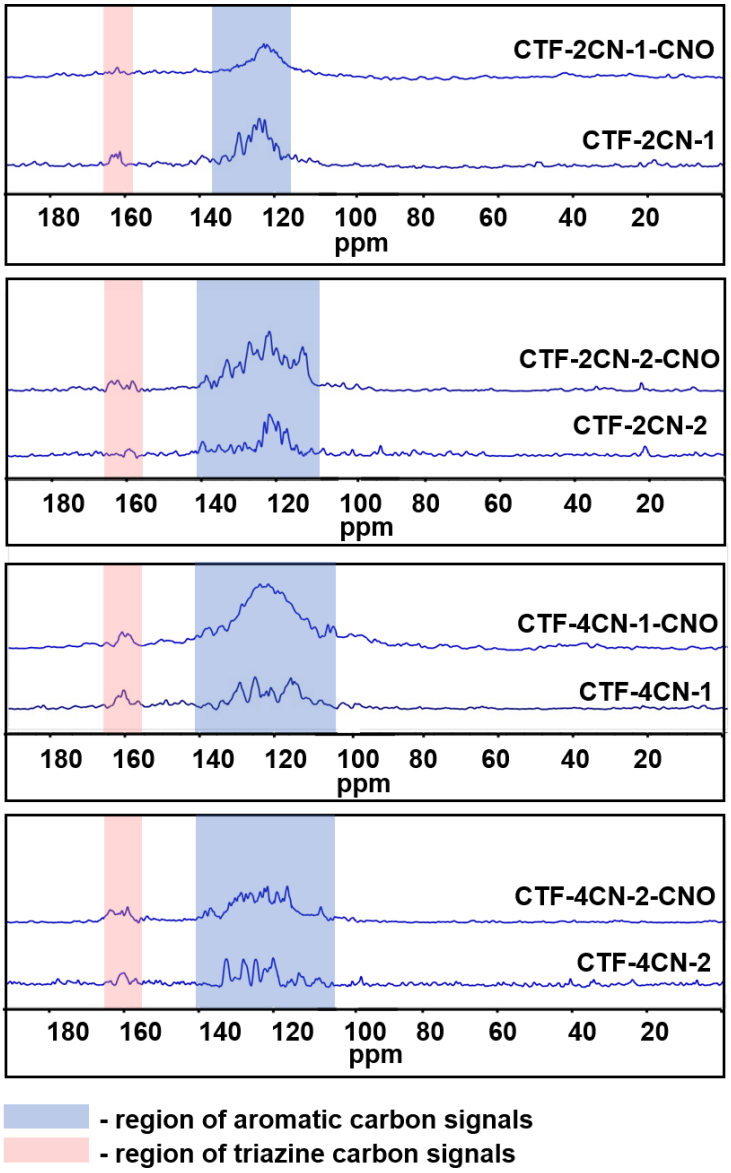

Figure S6. ^{13}C CP-MAS NMR spectra of the CTF and CTF-CNO materials.

Table S2. Chemical state, positions, FWHM, and relative area percentages of the deconvoluted C 1s peaks from the XPS analyses of CTF materials.

Region	Species	CTF-2CN-1			CTF-2CN-2			CTF-4CN-1			CTF-4CN-2		
		Peak (eV)	FWHM (eV)	% Area	Peak (eV)	FWHM (eV)	% Area	Peak (eV)	FWHM (eV)	% Area	Peak (eV)	FWHM (eV)	% Area
C 1s A	C-H sp^3	285.0	0.87	26.5	285.0	0.87	22.1	285.0	0.85	27.1	285.0	0.87	27.4
C 1s B	C=C sp^2	284.5	0.91	37.7	284.5	0.91	32.7	284.5	0.88	39.0	284.5	0.91	37.8
C 1s C	C-C sp^3	285.6	0.92	14.1	285.7	0.92	17.7	285.6	0.89	14.0	285.6	0.92	13.7
C 1s D	C=N	286.3	1.01	9.7	286.4	1.01	10.6	286.4	0.98	9.4	286.4	1.01	9.2
C 1s E	C-O-C	287.1	0.88	3.2	287.2	0.88	4.3	287.1	0.86	2.8	287.1	0.88	3.1
C 1s F	C=O	287.8	0.89	2.4	287.9	0.89	1.8	287.9	0.87	1.8	287.8	0.89	1.9
C 1s G	C-N	288.9	1.17	2.1	289.1	1.26	5.1	288.9	1.13	1.3	288.9	1.27	2.8
C 1s DCS	defects in carbon structure	283.8	0.80	4.4	283.9	0.85	5.7	283.9	0.86	4.7	283.8	0.86	4.0

Table S3. Chemical state, positions, FWHM, and relative % area of the deconvoluted C 1s peaks from the XPS analyses of CTF-CNO materials.

Region	Species	CTF-2CN-1-CNO			CTF-2CN-2-CNO			CTF-4CN-1-CNO			CTF-4CN-2-CNO		
		Peak (eV)	FWHM (eV)	% Area	Peak (eV)	FWHM (eV)	% Area	Peak (eV)	FWHM (eV)	% Area	Peak (eV)	FWHM (eV)	% Area
C 1s A	C-H sp^3	285.0	0.87	25.4	285.0	0.85	22.9	285.0	0.87	24.9	285.0	0.85	23.1
C 1s B	C=C sp^2	284.5	0.91	34.5	284.5	0.88	49.1	284.5	0.91	40.4	284.5	0.88	46.9
C 1s C	C-C sp^3	285.6	0.92	16.2	285.6	0.90	10.8	285.6	0.92	14.0	285.6	0.89	11.6
C 1s D	C=N	286.4	1.01	9.8	286.4	0.99	6.8	286.4	1.01	8.7	286.4	0.98	7.7
C 1s E	C-O-C	287.1	0.89	3.8	287.1	0.86	2.4	287.1	0.89	3.2	287.1	0.86	2.6
C 1s F	C=O	287.8	0.90	2.2	287.8	0.87	1.3	287.9	0.90	2.1	287.8	0.87	1.1
C 1s G	C-N	288.9	1.17	2.9	288.9	1.14	1.3	288.9	1.17	1.7	288.9	1.27	1.9
C 1s DCS	defects in carbon structure	283.9	0.78	5.3	283.8	0.79	5.7	283.9	0.86	5.1	283.8	0.78	5.1

Table S4. Chemical state, positions, FWHM, and relative area percentages of the deconvoluted N 1s peaks from XPS analyses of CTF materials.

Region	Species	CTF-2CN-1			CTF-2CN-2			CTF-4CN-1			CTF-4CN-2		
		Peak (eV)	FWHM (eV)	% Area	Peak (eV)	FWHM (eV)	% Area	Peak (eV)	FWHM (eV)	% Area	Peak (eV)	FWHM (eV)	% Area
N 1s A	triazine	398.3	1.47	38.3	398.4	1.47	31.3	398.3	1.48	41.2	399.0	1.44	38.4
N 1s B	pyrrolic	400.0	1.49	33.6	400.0	1.47	37.5	400.0	1.48	28.5	400.0	1.47	30.8
N 1s C	tertiary graphitic amine	401.2	1.49	23.6	401.2	1.49	24.4	401.2	1.48	23.3	401.1	1.47	25.0
N 1s D	quaternary graphitic amine	402.8	1.62	4.5	403.0	1.61	6.9	402.8	1.62	7.1	402.9	1.62	5.9

Table S5. Chemical state, positions, FWHM, and relative % area of the deconvoluted N 1s peaks from XPS analyses of CTF-CNO materials.

Region	Species	CTF-2CN-1-CNO			CTF-2CN-2-CNO			CTF-4CN-1-CNO			CTF-4CN-2-CNO		
		Peak (eV)	FWHM (eV)	% Area	Peak (eV)	FWHM (eV)	% Area	Peak (eV)	FWHM (eV)	% Area	Peak (eV)	FWHM (eV)	% Area
N 1s A	triazine	398.4	1.46	41.9	398.3	1.46	41.2	398.3	1.48	43.1	398.4	1.48	37.6
N 1s B	pyrrolic	400.0	1.47	32.6	400.0	1.46	31.2	400.0	1.46	34.0	400.0	1.49	31.3
N 1s C	tertiary graphitic amine	401.1	1.47	21.3	401.2	1.48	21.7	401.2	1.47	17.9	401.2	1.48	25.2
N 1s D	quaternary graphitic amine	402.9	1.61	4.1	402.8	1.61	6.0	402.9	1.63	5.1	402.9	1.62	5.9

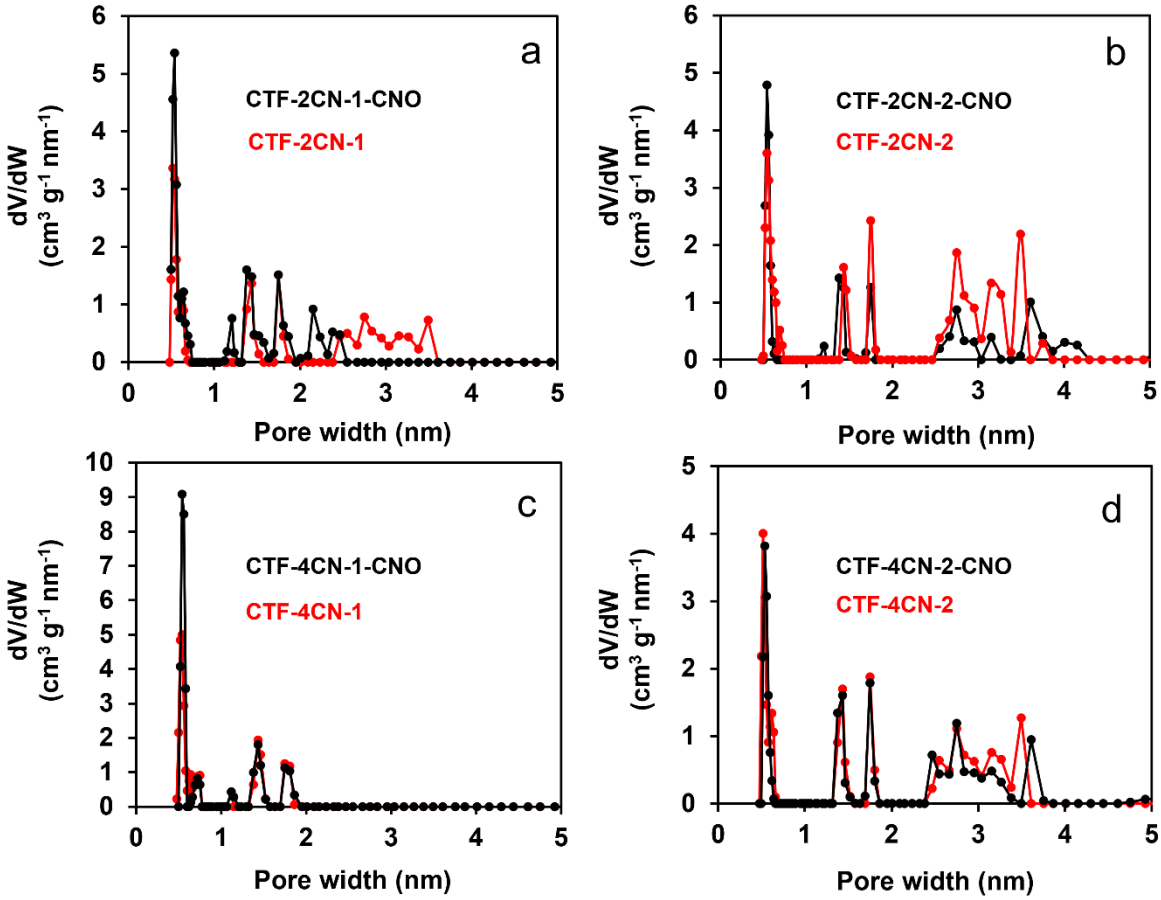

Figure S7. The differential nanopore size distribution of CTF and CTF-CNO materials.

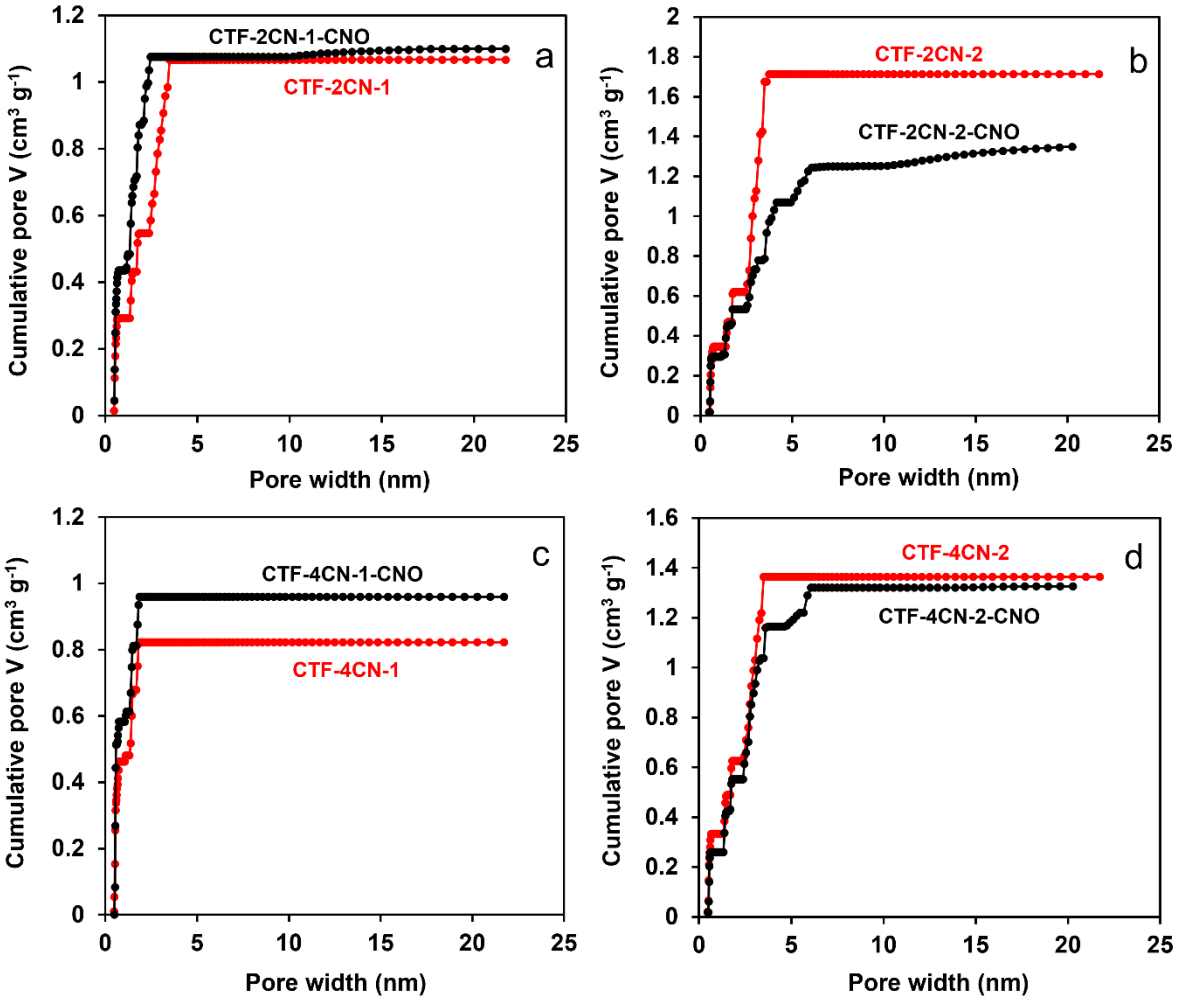

Figure S8. The cumulative nanopore volume of CTF and CTF-CNO materials.

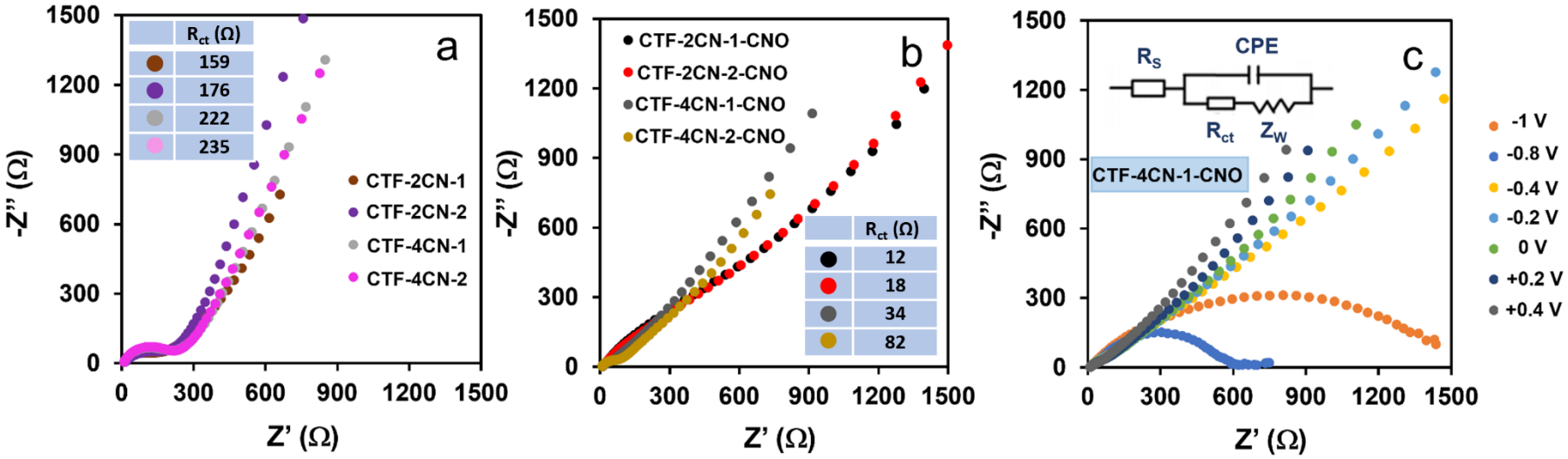

Figure S9. Nyquist plots obtained for GCE electrodes covered with (a) CTF and (b) CTF-CNO materials at 0.4 V. (c) EIS spectra recorded for GCE modified with **CTF-4CNO-1-CNO** at different potentials and electrical equivalent circuit (inset).

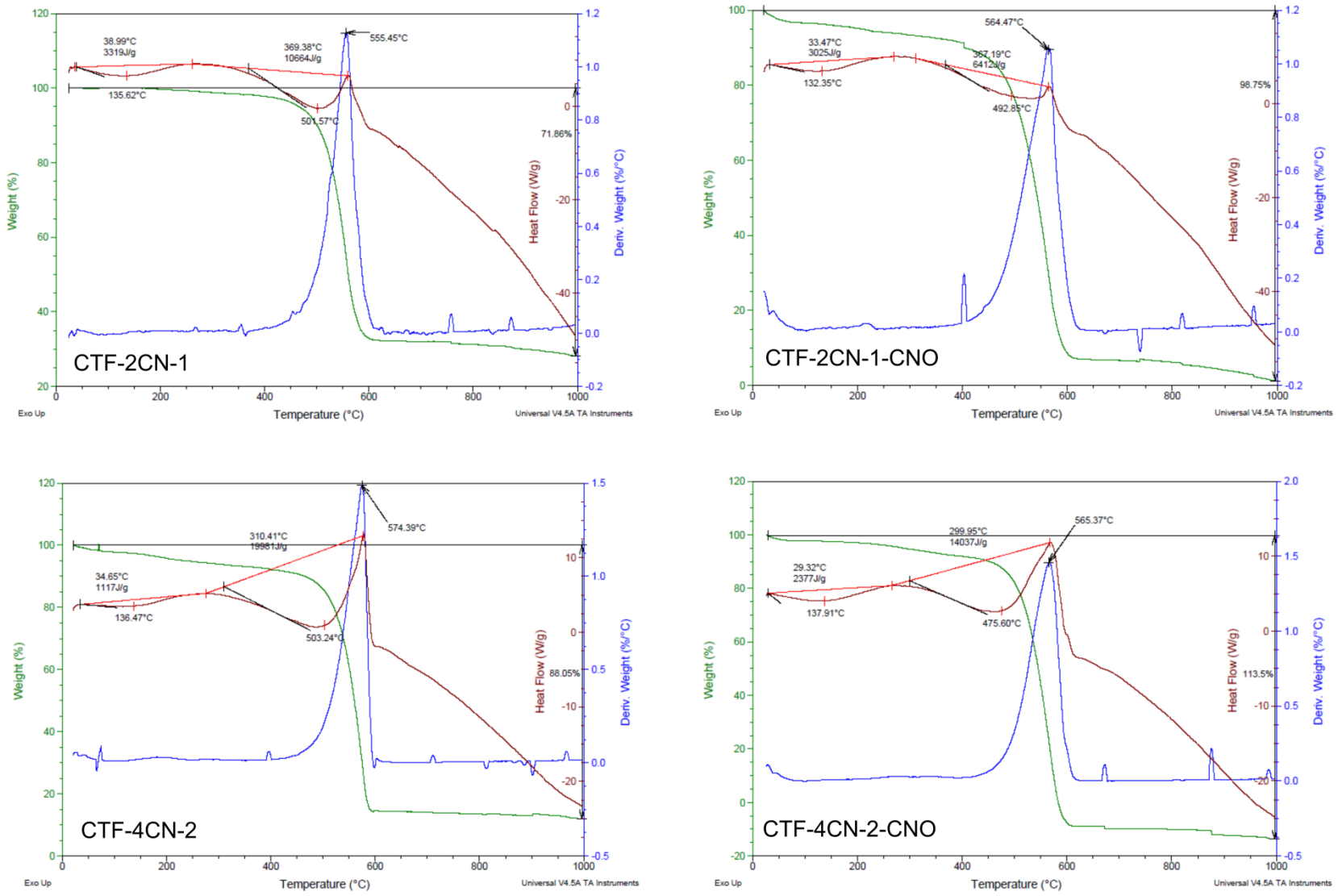

Figure S10. TGA/DSC analysis of the selected pristine CTF and CTF-CNO materials. Analysis was performed in an air atmosphere.

Table S6. Electrochemical properties of porous carbon materials containing triazine framework and their hybrids with carbon nanostructures.

Material/Precursor		Temperature of pyrolysis	Content of N (at%)	S_{BET} ($m^2 g^{-1}$)	Specific capacitance ($F g^{-1}$)		Ref.
					3-electrodes	2-electrodes	
Pristine CTF	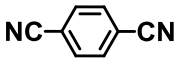 dicyanobenzene (terephtalonitrile)	600	11.8	1558	220	-	1
		700	8.2	2581	171	-	2
		400	12.44	1175	248	-	3
		450	11.06	1565	276	-	
		500	10.74	1681	285	-	
		550	9.26	1724	298	-	
		600	9.01	2197	263	-	
		650	7.77	2098	273	-	
		700	5.75	2237	243	-	
	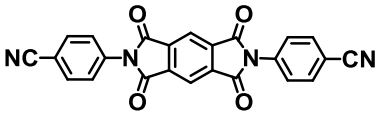 TIDN	550	-	1283	210	-	3
		600	-	-	231	-	
		650	-	-	202	-	
		700	-	1527	198	-	
	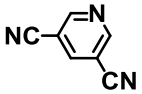 3,5-dicyanopyridine	400	28	680	-	0	4
		500	23.5	1120	-	0	
		600	15.8	1940	-	60	
		700	12.7	3120	-	141	
	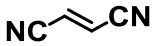 fumaronitrile	500	34.2	460	79	-	5
		600	25.8	443	187	-	
		700	20.9	1293	404	-	
		800	16.5	1234	143	-	
		900	14	1268	220	-	
	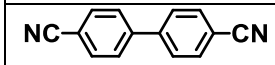 [1,1'-biphenyl]-4,4'-dicarbonitrile	600	4.7	1451	280	-	1

Pristine CTF	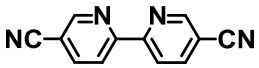 [2,2'-bipyridine]-5,5'-dicarbonitrile	600	11.3	2278	393	-	1
	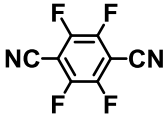 2,3,5,6-tetrafluoroterepthalonitrile	700	12.1	1849	326	115	6
		400	19.9	1345	379	-	7
	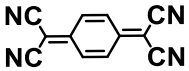 tetracyanoquinodimethane	800	8.13	3660	383	-	8
	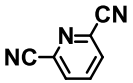 pyridine-2,6-dicarbonitrile	500	23.14	604	285.8	-	9
		600	21.09	1099	340.1	-	
		700	12.96	2316	363.3	-	
		800	11.82	2795	406	246	
		600	13	2230	324	-	1
	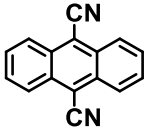 9,10-dicyanoanthracen	400	-	406	435	-	10
		500	-	751	589	-	
	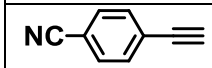 polyethynylbenzonitrile	800	5.8	1954	628	-	11
	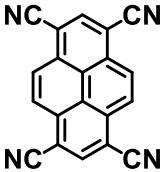 1,3,6,8-tetracyanopyrene	500	-	1019	500	-	12

Pristine CTF	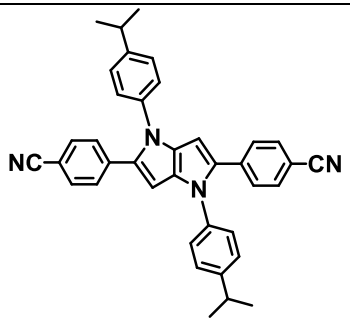 2CNPP	500 600 700	1.6 4.3 6.4	1371 1527 1052	187 197 255	- - -	13
	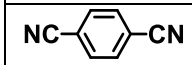 2CN-1 (terephtalonitrile)	700	6.6	1612	200	81 (8 A g^{-1})	
	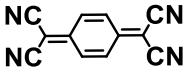 4CN-1 (tetracyanoquinodimethane)	700	7.5	1835	269	114 (8 A g^{-1})	
	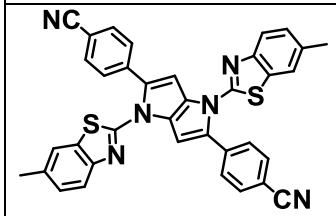 2CN-2	700	5.4	2260	303	133 (8 A g^{-1})	**this study**
	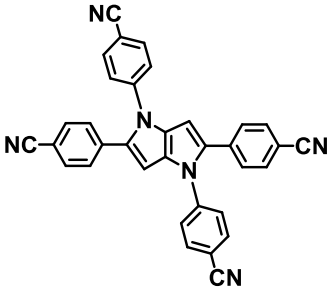 4CN-2	700	6.5	1962	291	123 (8 A g^{-1})	

CTF-carbon nanostuctures hybrids	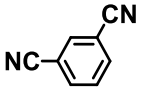 *m*-phtalodinitrile and graphene oxide	800	6.3	1268.5	325	-	14
	2CNPP and CNOs	600 700	4.5 3.6	1054 2694	375 638	- -	13
	2CN-1 and CNOs	700	8.1	2143	376	131 (8 A g^{-1})	**this study**
	4CN-1 and CNOs	700	9.5	2126	498	302 (2 A g^{-1}) 237 (8 A g^{-1})	
	2CN-2 and CNOs	700	4.8	1625	472	205 (8 A g^{-1})	
	4CN-2 and CNOs	700	4.3	1786	417	171 (8 A g^{-1})	

References

(1) Zhang, Y.; Zhang, B.; Chen, L.; Wang, T.; Di, M.; Jiang, F.; Xu, X.; Qiao, S. Rational Design of Covalent Triazine Frameworks Based on Pore Size and Heteroatomic Toward High Performance Supercapacitors. *J. Colloid Interface Sci.* **2022**, *606*, 1534–1542. https://doi.org/10.1016/j.jcis.2021.08.087.

(2) Baumann, D.; Lee, C.; Wan, C.; Sun, H.; Duan, X. Hierarchical Porous Carbon Derived from Covalent Triazine Frameworks for High Mass Loading Supercapacitors. *ACS Materials Lett.* **2019**, *1*, 320–326. https://doi.org/10.1021/acsmaterialslett.9b00157.

(3) Hao, L.; Luo, B.; Li, X.; Jin, M.; Fang, Y.; Tang, Z.; Jia, Y.; Liang, M.; Thomas, A.; Yang, J.; Zhi, L. Terephthalonitrile-Derived Nitrogen-Rich Networks for High Performance Supercapacitors. *Energy Environ. Sci.* **2012**, *5*, 9747–9751. https://doi.org/10.1039/C2EE22814A.

(4) Troschke, E.; Leistenschneider, D.; Rensch, T.; Grätz, S.; Maschita, J.; Ehrling, S.; Klemmed, B.; Lotsch, B. V.; Eychmüller, A.; Borchardt, L.; Kaskel, S. In Situ Generation of Electrolyte inside Pyridine- Based Covalent Triazine Frameworks for Direct Supercapacitor Integration. *ChemSusChem* **2020**, *13* (12), 3192–3198. https://doi.org/10.1002/cssc.202000518.

(5) Wang, D.-G.; Wang, H.; Lin, Y.; Yu, G.; Song, M.; Zhong, W.; Kuang, G.-C. Synthesis and Morphology Evolution of Ultrahigh Content Nitrogen-Doped, Micropore-Dominated Carbon Materials as High-Performance Supercapacitors. *ChemSusChem* **2018**, *11* (22), 3932–3940. https://doi.org/10.1002/cssc.201801892.

(6) Gao, Y.; Cui, P.; Liu, J.; Sun, W.; Chen, S.; Chou, S.; Lv, L.-P.; Wang, Y. Fluorine/Nitrogen Co-Doped Porous Carbons Derived from Covalent Triazine Frameworks for High-Performance Supercapacitors. *ACS Appl. Energy Mater.* **2021**, *4* (5), 4519–4529. https://doi.org/10.1021/acsaem.1c00155.

(7) Gao, Y.; Zhi, C.; Cui, P.; Zhang, K. A. I.; Lv, L.-P.; Wang, Y. Halogen-Functionalized Triazine-Based Organic Frameworks Towards High Performance Supercapacitors. *Chem. Eng. J.* **2020**, *400*, 125967. https://doi.org/10.1016/j.cej.2020.125967.

(8) Li, Y.; Zheng, S.; Liu, X.; Li, P.; Sun, L.; Yang, R.; Wang, S.; Wu, Z.-S.; Bao, X.; Deng, W.-Q. Conductive Microporous Covalent Triazine-Based Framework for High-Performance Electrochemical Capacitive Energy Storage. *Angew. Chem. Int. Ed.* **2018**, *57*, 7992–7996. https://doi.org/10.1002/anie.201711169.

(9) Wu, C.; Zhang, H.; Hu, M.; Shan, G.; Gao, J.; Liu, J.; Zhou, X.; Yang, J. In Situ Nitrogen-Doped Covalent Triazine-Based Multiporous Cross-Linking Framework for High-Performance Energy Storage. *Adv. Electron. Mater.* **2020**, *6* (7), 2000253. https://doi.org/10.1002/aelm.202000253.

(10) Mohamed, M. G.; Sharma, S. U.; Liu, N.-Y.; Mansoure, T. H.; Samy, M. M.; Chaganti, S. V.; Chang, Y.-L.; Lee, J.-T.; Kuo, S.-W. Ultrastable Covalent Triazine Organic Framework Based on Anthracene Moiety as Platform for High-Performance Carbon Dioxide Adsorption and Supercapacitors. *Int. J. Mol. Sci.* **2022**, *23*. https://doi.org/10.3390/ijms23063174.

(11) Vadiyar, M. M.; Liu, X.; Ye, Z. Macromolecular Polyethynylbenzonitrile Precursor-Based Porous Covalent Triazine Frameworks for Superior High-Rate High-Energy Supercapacitors. *ACS Appl. Mater. Interfaces* **2019**, *11*, 45805–45817. https://doi.org/10.1021/acsami.9b17847.

(12) Mohamed, M. G.; EL-Mahdy, A. F. M.; Takashi, Y.; Kuo, S.-W. Ultrastable Conductive Microporous Covalent Triazine Frameworks Based on Pyrene Moieties Provide High-Performance CO_2 Uptake and Supercapacitance. *New J. Chem.* **2020**, *44*, 8241–8253. https://doi.org/10.1039/D0NJ01292K.

(13) Hryniewicka, A.; Breczko, J.; Siemiaszko, G.; Papathanassiou, A.; Góra-Marek, K.; Tarach, K. A.; Brzezinski, K.; Ilnicka, A.; Terzyk, A. P.; Markiewicz, K. H.; Echegoyen, L.; Plonska-Brzezinska, M. E. Pyrrolo[3,2-b]Pyrrole-Based Covalent Triazine Framework: Three-Dimensional Organization of Pores Using Nanostructural Spherical Carbon. *Chem RXiv* **2022**. https://doi.org/10.26434/chemrxiv-2022-h0n3l.

(14) Peng, L.; Guo, Q.; Ai, Z.; Zhao, Y.; Liu, Y.; Wei, D. Nitrogen Doped Carbons Derived From Graphene Aerogel Templated Triazine-Based Conjugated Microporous Polymers for High-Performance Supercapacitors. *Front. Chem.* **2019**, *7*, 142. https://doi.org/10.3389/fchem.2019.00142.